Tailoring cryo-electron microscopy grids by photo-micropatterning for in-cell structural studies

Mauricio Toro-Nahuelpan[1], **Ievgeniia Zagoriy**[1], **Fabrice Senger**[2], **Laurent Blanchoin**[2,3], **Manuel Théry**[2,3], **Julia Mahamid**[1,*]

[1]Structural and Computational Biology Unit, European Molecular Biology Laboratory, Heidelberg, Germany

[2]CytomorphoLab, Interdisciplinary Research Institute of Grenoble, Laboratoire de Physiologie Cellulaire et Végétale, Université Grenoble-Alpes/CEA/CNRS/INRA, Grenoble, France

[3]CytomorphoLab, Hôpital Saint Louis, Institut Universitaire d'Hématologie, Université Paris Diderot, Paris, France

Abstract

Spatially-controlled cell adhesion on electron microscopy (EM) supports remains a bottleneck in specimen preparation for cellular cryo-electron tomography. Here, we describe contactless and mask-free photo-micropatterning of EM grids for site-specific deposition of extracellular matrix (ECM)-related proteins. We attained refined cell positioning for micromachining by cryo-focused ion beam milling. Complex micropatterns generated predictable intracellular organization, allowing direct correlation between cell architecture and *in-cell* 3D-structural characterization of the underlying molecular machinery.

In parallel to the ongoing resolution revolution in cryo-electron microscopy for macromolecular structure determination[1], cryo-electron tomography (ET) has matured to reveal the molecular sociology *in situ sensu stricto* [2–4]. Yet, molecular-resolution cryo-ET of adherent mammalian cells can only be directly performed on their thin peripheries (< 300 nm). To reveal structures at the cell interior, thinning by cryo-focused ion beam (FIB) has proved an optimal, artifact-free preparation method[2,5–12]. Thus, cryo-FIB micromachining coupled to cryo-ET, followed by subtomogram averaging[13,14], allows the capture of conformational states and function-related assemblies of macromolecules *in cellulo* [4,11,15]. Specimen preparation for cellular cryo-ET, whether performed directly on thin cellular

*Corresponding author. julia.mahamid@embl.de.

peripheries or following cryo-FIB micromachining, involves seeding of adherent cells on EM grids made of a biocompatible metal (e.g. gold). Standard EM grids are 3 mm diameter metal meshes overlaid with a delicate perforated thin film. Cells are typically allowed to spread, subjected to genetic or molecular perturbation to represent different physiological settings to be examined in molecular detail, that are then arrested by vitrification[2]. However, for cells to be thinned by cryo-FIB, they must be positioned roughly at the center of an individual grid square (Fig. 1a)[6], and within a few squares away from the grid center. Whilst the first requirement is necessary to allow access to cellular material for ablation by the FIB, the restriction of specimen positioning to the central area of the grid is posed by the subsequent requirement of stage tilt in the transmission electron microscope (TEM) for collection of tomographic tilt-series.

Despite a growing number of successfully reported *in-cell* cryo-ET studies[4,9,15–18], controlled on-grid positioning of adherent mammalian cells has remained largely unaddressed. Currently, optimization of grids for cellular cryo-ET is primarily carried out by adjusting the concentration of the cell suspension during seeding. Some efforts have also been made by functionalizing grids with ECM-related proteins to promote adhesion of various cell types[19–24]; however, adherent cells settle and spread randomly on the homogenously coated grid films, often in the vicinity or directly on the metal grid bars, making them inaccessible to the FIB or to cryo-ET (Fig. 1a). Furthermore, the presence of large clusters of cells increases the chance of incomplete vitrification due to slower heat transfer from the larger mass of material, and thus deteriorate structural preservation. Such technical hurdles have made the application of state-of-the-art cellular cryo-ET challenging. They further limit the advance of technical developments towards automation and high-throughput sample preparation. Here, we adapted photo-micropatterning, routinely applied to centimeter-scale glass slides for light microscopy-based assays[25,26], to develop functionalized EM supports for directing cell positioning at high spatial accuracy, which ultimately render molecular-resolution imaging of frozen-hydrated specimens more easily attainable.

We employed contactless and mask-free photo-micropatterning (Supplementary Fig. 1), ensuring preservation of the delicate support film and precise pattern generation within each grid square. The grids were plasma cleaned, rendering them hydrophilic, and coated with an anti-fouling biologically repelling agent (Polyethylene glycol (PEG)-brush, Supplementary Fig. 1a). Successively, specific areas were ablated with a UV-laser, either using a UV-pulsing laser scanned through the grid film on a standard confocal microscope (Supplementary Fig. 1b, Supplementary Fig. 2a-d) or continuous UV-illumination with a digital micro-mirror device (DMD) and a photo-activator (PLPP)[27] (Supplementary Fig. 1b'). The DMD provides efficient area coverage of the grid film of approximately 150,000 μm^2, equivalent to about 3 x 2 grid squares on a 200-mesh grid, and allows creating multiple, complex, and precisely positioned PEG-oxidized areas in ~30 s at a resolution of 1.2 μm. The total patterned area can be extended by iterative montages of DMD expositions (Supplementary Fig. 3). Following passivation and patterning, grids can be stored up to 30 days under hydrated conditions at 4°C. Grids were then functionalized with proteins that facilitated cell adhesion (Supplementary Fig. 1d-e), and can be tailored to support growth and differentiation of various cell types. We demonstrate successful patterning on a variety of

grid materials for both the metal mesh and support film (see Supplementary Fig. 3 and Supplementary Discussion for a detailed description). For example, we replaced the commonly used holey amorphous carbon by SiO_2 films[12,24] (Supplementary Fig. 3a-c), or used an additional layer of thin (2 nm) continuous carbon (on a carbon holey film) to potentially allow for continuous large areas to support cell adhesion (Supplementary Fig. 3d). We also utilized titanium grids (Supplementary Fig. 3e) instead of the typical gold grids. Titanium provided more rigid grids, that combined to SiO_2 films, proved to maintain flatness (avoiding cryo-crinkling[28]), and were more robust for the multiples steps during the micropatterning and cell culture steps (see Online Methods). Alternatively, all-gold grids (mesh and film, Supplementary Fig. 3f-k) were also successfully patterned and supported cell culture.

HeLa cells are a prominent model system in cell biology, and must be thinned to reveal structures positioned deep in their interior by cryo-ET. HeLa cells were seeded on fibronectin-functionalized micropatterned (30 μm disk-shape) grids. Reproducible seeding of one or two cells at the center of individual grid squares was achieved (Fig. 1b, Supplementary Fig. 2e-g, Supplementary Fig. 3b,c,g-j). Cell viability on micropatterned grids was confirmed by live-cell imaging: time-lapse light microscopy of cell-cycle synchronized cultures showed that cells spread and continue to divide 40 h post-seeding (Fig. 1c-d, Supplementary Video 1). In this case, an H-shape pattern induced cells to adopt a rectangular appearance and can potentially be employed to produce defined geometries of cell division and of the mitotic spindle for structural analysis[29,30]. The majority of cells seeded on such grids were directly accessible for FIB thinning (Fig. 1b, e), highlighting the potential of grid micropatterning in streamlining advanced thinning techniques. The presence of microbeads on the grid (Fig. 1e), aimed to be used as fiducials for 3D cryo-correlative light and electron microscopy (CLEM)[31], demonstrates that 3D-targeted FIB preparations could also benefit from spatially-controlled cell positioning. Next, electron-transparent lamellae were generated (Fig. 1f, Supplementary Fig. 2g-h)[6], and cryo-ET on the lamellae produced 3D-tomographic volumes of the nuclear periphery capturing previously-described molecular detail[4] (Fig. 1g). Thus, the developed EM grid micropatterning method offers important advantages for optimization of advanced cellular cryo-ET pipelines, which encompass (i) vitrification, (ii) cryo-CLEM, (iii) micromachining by cryo-FIB milling, and (iv) cryo-ET.

Next, we generated complex patterns to control cell shape. Micropatterning on glass surfaces has been previously shown to induce well-defined cytoskeletal architectures and, as a result, a stereotypical internal organization of the cellular cytoskeleton, as well as organelles[25,26]. Here, we describe the actin network in Retinal pigment epithelium (RPE1) cells as a proof of principle and a case of study, which provides a direct readout of the cellular response to adhesion on complex patterns. Complex micropatterns induced reproducible cell morphologies on grids (Fig. 2a)[32]. Each pattern elicited a distinguishable actin 3D architecture[26,33,34], with spatially distinct peripheral and internal stress fibers, transverse arcs and isotropic branched meshworks. To elucidate the actin organization underlying these architectures, we first performed cellular tomography directly on the thin peripheries of micropattern-shaped cells (Fig. 2b, Supplementary Fig. 4). A cell grown on a cross-shaped micropattern (Fig. 2c) was chosen aiming to target peripheral actin stress fibers as indicated

by the live-cell actin map (Fig. 2a, upper-left). Cryo-TEM of the selected region exhibited a peripheral cellular protrusion and a noticeable stress fiber (Fig. 2d, Supplementary Fig. 5a-d. See Supplementary Fig. 5e-k for additional examined cells). Cryo-ET on the targeted area revealed the presence of a peripheral bundle of aligned actin filaments comprising a stress fiber and the cortical meshwork of a cellular protrusion (Fig. 2e, Supplementary Video 2). Cryo-ET on a different, natively thinner, cell periphery displayed a meshwork of individual actin filaments, exhibiting the expected helical structure (Fig. 2f, Supplementary Fig. 5l-m, Supplementary Video 3). Hexameric macromolecular complexes observed in the vicinity of the basal and apical cell membranes resemble previously reported adhesion-related particles[17] (Fig. 2f, inset).

To explore the organization of the cytoskeleton further away from the cell peripheries and to characterize spatially-predictable structures according to live-cell actin maps (Supplementary Fig. 6a b), we further applied cryo-FIB milling to the micropattern-adherent RPE1 cells. Cryo-scanning electron microscopy (SEM) of a patterned grid shows the accurate single cell positioning at the centers of individual grid squares (Fig. 2g). Multiple different patterns can be generated on the same grid for direct comparison of different cellular architectures. The patterns' design can be easily identified by direct imaging with low-voltage SEM or the micropattern-adopted cell shape (Fig. 2g, bottom panels), facilitating the overlay of the pattern design (Fig. 2g, top). An adherent RPE1 cell on a crossbow-shape micropattern was selected for thinning by means of cryo-FIB micromachining (Fig. 2h). The majority of the cell material was removed using a single rectangular area (Fig. 2i). This ablates the top of the cell, generating a thin wedge at the basal cell membrane[6]. Cryo-ET at positions 1 and 2, indicated on the wedge (Fig. 2h), displayed a curved transverse arc and a stress fiber, respectively (Fig. 2j-k, Supplementary Fig. 6c-e, Supplementary Video 4, and Supplementary Fig. 7a-d). Furthermore, microtubules were seen parallel to and, remarkably, fully embedded in the actin stress fiber (Fig. 2k). These structures matched the previously described actin organization in crossbow patterns[33], in which the observed actin bundles likely form part of the transverse arcs, while microtubules were suggested to be aligned with stress fibers at the basal part of the cell (Fig. 2a, upper-right). Thus, this approach provided novel biological insights, previously described by light microscopy, but only hereby unambiguously confirmed by direct visualization of distinct cytoskeleton architectures induced by control of cell morphology *in cellulo*. Further data processing by semi-automated segmentation of the tomographic volumes can deliver quantitative 3D structural information, including angular distributions of individual actin filaments and inter-filament distances in different cytoskeletal architectures, a level of structural information that is uniquely attainable by cryo-ET[35]. We further envision that the reproducible internal organization, encompassing positioning of cytoskeletal elements and stereotypical organelles organization in response to predetermined external physical cues posed by the micropatterns (Supplementary Fig. 6f)[33], will assist in targeting specific internal elements for structural studies without resorting to challenging correlative approaches under cryogenic conditions.

In conclusion, photo-micropatterning of EM grids contributes to the advancement of refined, routine and user-friendly specimen preparations for *in-cell* structural biology. It further aids in solving technical challenges that have, thus far, hindered high-throughput FIB thinning

preparations. This method has great potential for developing automation of the cryo-FIB milling process, deeply impacting the streamlining of the cellular cryo-EM pipeline. It offers a unique opportunity to generate *in-cell* integrated insight into the structure and dynamics of macromolecules at nanometer-scale, broadening the scope of questions that can be addressed by state-of-the-art structural biology methods and bridging to other life-science disciplines.

Online Methods

A Supplementary Protocol detailing the method reported here is available[36].

Cell lines and culture

Wild type HeLa Kyoto cells, and a double tagged line expressing both green fluorescent protein (GFP)-tagged β-tubulin from a bacterial artificial chromosome (BAC) and mCherry tagged histone from a plasmid construct (H2B-mCherry), were kindly provided by the Hyman Lab, Max Planck institute of Molecular Cell Biology and Genetics. HeLa cells were cultured in Dulbecco's modified Eagle's medium (DMEM GlutaMAX; ThermoFischer Scientific, Schwerte, Germany), while RPE1 (Retinal Pigment Epithelial human cells) expressing LifeAct-GFP[37] were cultured in DMEM F-12 GlutaMAX. Cells were incubated at 37°C with 5 % CO_2, and supplemented with 10 % (v/v) fetal bovine serum (FBS), 100 mg/mL penicillin, 100 mg/mL streptomycin. A 0.5 mg/mL geneticin (G418) for the BAC-tagged lines and Puromycin (1 μg/ml) for cells carrying the plasmids were used. FluoroBrite DMEM supplemented with 2mM L-glutamine (ThermoFischer Scientific, Schwerte, Germany) was used for live cell fluorescence imaging.

Electron microscopy grids

Gold (Au) mesh grids with either a holey 12 nm thick film made of SiO_2 (R1.2/20, R1/4, hole size/spacing in μm), amorphous carbon (R2/1), or 50 nm gold film (UltrAuFoil®, R2/2) were used. A gold mesh with a continuous thin layer (2 nm) of amorphous carbon placed on top of a holey (R2/1) carbon film was also employed. In addition, we used titanium (Ti) grids with a holey (R1.2/20) 12 nm thick SiO_2. All grids were 200-mesh and purchased from Quantifoil Micro Tools, Jena, Germany. For detailed description of the different grid materials for mesh and support, see Supplementary Discussion.

Grid passivation

One-step—Grids were oxidized and rendered hydrophilic using a low-pressure plasma cleaning (Diener Femto Plasma. Diener electronic, Ebhausen, Germany). Grids were placed onto a glass slide and both sides were plasma cleaned at 100 W power with a 10 cm^3/min flow rate of oxygen gas for 30-40 s. Next, grids were incubated on droplets of poly-L-lysine grafted with polyethylene glycol (PLL(20)-g[3.5]-PEG(5), SuSoS AG, Dübendorf, Switzerland) at a concentration of 0.5 mg/ml in 10 mM Hepes pH 7.4, for 1h at room temperature or overnight at 4°C, on parafilm in a humid chamber (parafilm sealed dish with soaked filter paper). Following passivation, the grids were blotted with filter paper from the back, allowed to dry for few seconds, and immediately placed on a drop of the next micropatterning solution (depending on the micropatterning method) in a sealed glass bottom ibidi μ-Dish 35 mm low (ibidi, Martinsried, Germany).

Two-step—As an alternative, a two-step treatment of the grids was also tested. First, grids were plasma cleaned, and then incubated on droplets of 0.01 % PLL (Sigma Aldrich, St. Louis, MO) on parafilm in a humid chamber overnight at room temperature. Next, the grids were rinsed five times in 100 mM $NaHCO_3$ pH 8.4, and incubated for 1-2 h with 50 mg/ml PEG-sva dissolved in the same solution (Laysan Bio, Arab, US). Subsequently, the grids were washed five times in 100 mM $NaHCO_3$ pH 8.4. This treatment can be potentially applied in the absence of a plasma cleaner.

Both protocols were successful for grid passivation followed by photo-micropatterning, as judged from fluorescence light microscopy imaging of GFP-adsorption that was restricted to the PEG-free patterns. However, a one-step PLL-g-PEG passivation was preferred for time consideration.

Micropattern design—Micropatterns were designed in Inkscape (http://www.inkscape.org/) as 8-bit binary files and exported as png files, which can be loaded into the Leonardo software v4.12 (Alvéole Lab, Paris, France).

Micropatterning and functionalization of grids

Nanoablation by a 355 nm pulse laser—An inverted confocal Olympus FluoView 1200 (Olympus, Hamburg, Germany) microscope was used, equipped with a UV pulsed laser source of 355 nm (PNV-001525-140, Teem Photonics, Meylan, France), a UPLSAPO 63x (NA 1.35) oil objective, and a standard PMT or GaAsP PMT detectors. The 355 nm laser had an average power of 50 mW, 500 ps pulse width, 1kHz repetition rate, and a maximum energy per pulse of 30 μJ. After passivation with PLL-g-PEG, grids were blot-dried from the back with a filter paper and quickly placed with the SiO_2 film facing down (towards the objective) on 1-3 μl of Hepes 10 mM pH 7.4 or PBS in a sealed glass bottom ibidi μ-Dish 35 mm low (ibidi, Martinsried, Germany). High humidity was kept using water-soaked filter paper inside the dish to avoid solution evaporation during micropatterning. Transmission and reflection were observed with a 488 nm laser. The patterns (ROIs) were of square or circular shape (20, 30 or 40 μm diameter) generated using the Olympus FV 10-ASW software v04.02.03.02. Photo-micropatterning was performed using 10-11 % laser power, 40 μs per pixel and 10 iterations. Individual grid squares were targeted at a time, the film focused and the laser applied. Micropatterning of a 4 x 4 grid squares area (200-mesh grid: ~260,000 $μm^2$) took approximately 8 min. Potentially, a lower magnification objective can be used in order to pattern more grid squares at the same time in order to optimize patterning, provided that the film is flat and at even height to maintain all areas in the focus plane. Titanium grids had a consistent film flatness aiding quick focusing on each grid square, facilitating the micropatterning using this technique.

PRIMO™ (DMD-based illumination + Photo-activator)—An inverted Nikon microscope Ti-E equipped with a CFI Super Plan FLuor 20x ELWD (NA 0.45) lens with high UV-transmission, a Perfect Focus System 3, an ORCA-Flash 4.0 LT CMOS camera (Hamamatsu, Japan), a motorized stage (Märzhäuser, Wetzlar, Germany), and the Primo™ micropatterning module (Alvéole Lab, Paris, France) was used. Grid micropatterning was performed using digital mirror device (DMD) to generate a spatially controlled laser

illumination of the sample (Primo™, Alvéole Lab, Paris, France), with a resolution limit of ~1.2 μm. After passivation with PLL-g-PEG, grids were blot-dried from the back with a filter paper and quickly placed on a 1-3 μl of PLPP (4 benzoylbenzyl-trimethylammonium chloride, 14.5 mg/ml) drop in a sealed glass bottom ibidi μ Dish 35 mm low (ibidi, Martinsried, Germany). High humidity was kept using water-soaked filter paper inside the dish to avoid PLPP evaporation. The dish, with 1-4 grids at a time, was placed on the microscope stage and photo-patterning was controlled with the μmanager software v1.4.22 by the Leonardo plugin software v4.12 (Alvéole Lab, Paris, France) using the stitching mode and a 375 nm (4.5 mW) laser, applying a dose of 800 1000 mJ/mm^2 equivalent to ~30 s per DMD exposition. Micropatterning of 8 x 7 grid squares area (200-mesh grid: ~900,000 μm^2) took 3-7 min depending on the total dose and grid positioning with respect to the DMD mirror illumination. Grids were promptly retrieved from the PLPP solution, washed in a 1,000 μl drop of water, and two consecutive washes in 300 μl drops of PBS. Patterned one-step passivated grids were stored wet in PBS at 4°C in a humid chamber, remaining functional for at least 30 days.

Grid functionalization—For functionalization following PEG ablation in micropatterns using both methods, grids were incubated at room temperature for 1h in a 20 μl drop of either 100 μg/ml of GFP, 50 μg/ml fibronectin (ThermoFischer Scientific, Schwerte, Germany), or 30 μg/ml of fibrinogen-Alexa546 (ThermoFischer Scientific, Schwerte, Germany) on parafilm and, subsequently, washed 3 times in 300 μl drops of PBS. Fibrinogen was prepared in 100 mM NaHCO$_3$ pH 8.4, hence washes were performed in the same buffer. Grids incubated with fibronectin remained functional for at least 10 days in PBS at 4°C in a humid chamber. The maximum active life time of the micropatterned grids, as well as protein functionalization remain unknown, as this will also depend on the protein stability itself.

All patterning steps and grid treatments were performed under sterile conditions using a Bunsen burner. Grids were handled with a tweezer n° 55 (Dumont, Montignez, Switzerland).

Comparison between the two patterning approaches—Due to the pulsing nature of the laser in the first approach, it has to scan the region of interest in order to ablate the anti-fouling agent. The action of the laser leaves an impression on the film that is visible by light microscopy (Supplementary Fig. 2a-b). The engraving can be further observed in detail by FIB (side view) and SEM (top view) imaging of a grid square (Supplementary Fig. 2c-d). Importantly, the film engraving at the conditions used did not seem to cause a deterioration of the SiO$_2$ layer. In fact, proper cell adhesion to the fibronectin-coated patterns (Supplementary Fig. 2e-f) and the subsequent vitrification of grids appeared unaltered (Supplementary Fig. 2g). Furthermore, followed by cell settling on the patterns, they strictly adhere and divide on the micropatterned regions (Supplementary Fig. 2f), denoting cell viability and the effectiveness of the passivation. Some agglomeration of cells can be appreciated in the Supplementary Fig. 2e. This can be overcome by optimizing cells seeding conditions using fewer cells/cm^2 and less time of seeding (earlier transfer to a new cell-free dish) along with use of a cell strainer. Using this method, a directed spatial positioning of cells was attained, which was valuable for cryo-FIB milling (Supplementary Fig. 2g-j),

demonstrating and further supporting the advantages of micropatterning for the cellular cryo-ET pipeline optimization.

Timing: while the Primo device takes 30 s per DMD run (for a dose of 1000 mJ/mm^2 and covering a 3 x 2 grid squares on a 200-mesh grid), the 355 nm-pulse laser patterning takes ~10-15 s per grid square considering a disk-shaped pattern of 20-30 μm diameter. A user familiar with the 355 nm laser technique can pattern a 4 x 4 grid square area in ~8 min, while the Primo technology covers a similar area in ~1 min.

Resolution: the 355 nm-pulse scanning laser can yield a much higher spatial lateral resolution limited by the light diffraction limit equivalent to ~250 nm, in comparison to the Primo performance that is limited to ~1.2 μm.

Cell seeding

Non-patterned grids were plasma cleaned. Cells were detached from cell culture flasks using 0.05 % trypsin-EDTA and seeded on pre-treated (either patterned or non-patterned) grids in glass bottom ibidi μ-Dish 35 mm high (ibidi, Martinsried, Germany).

Cells were seeded on fibronectin micropatterned surfaces right after being passed through a cell 40 μm pore-size cell strainer (Corning, Amsterdam, Netherlands) at a density of 2×10^4 cells/cm^2 for HeLa and 8×10^3 cells/cm^2 for RPE1 cell lines. After seeding, grids were incubated for 1.5-2 h for HeLa cells or 20-35 min for RPE1 cells. Next, grids were transferred to a new cell-free dish and incubated at 37°C with 5 % CO$_2$ to allow cell adhesion to the grids. Transfer to a new dish was beneficial to remove cells that were non-specifically attached to areas outside the patterns. Cells were vitrified 4-6 h post-transfer for RPE1 cells (to attain a higher number of grid squares with single cells) or after overnight incubation for HeLa cells.

At least 60 grids have been seeded with either HeLa or RPE1 cells obtaining reproducible results with cells settling and adhering to the micropatterned areas.

Live-cell confocal imaging

Cell-cycle synchronization was aimed at validating cell viability after adhesion on micropatterned grids by live cell imaging. HeLa cells were allowed to adhere overnight (16 h) in the presence of 2 mM Thymidine (S-phase block; Merck, Darmstadt, Germany) and released into fresh medium. Imaging started 8h post-release and time-lapse movies were recorded overnight.

Time lapse imaging of HeLa cells on grids (Fig. 1c, d) was performed on a Zeiss LSM 880 Airyscan microscope (Carl Zeiss, Jena, Germany) using confocal detectors and a Plan-Apochromat 20x (NA 0.8) objective. Field of view: 425 x 425 μm^2. Pixel size of 149 nm, and 1 μm as *z*-step (total z-depth: 32 μm). Pixel dwell time: 0.28 μs. Master gain 850 for both channels. GFP was detected using a 488 nm line of Argon laser with a 1.5 % power and a 490-550 nm bandpass emission filter. mCherry was detected using a 561 nm DPSS laser at a 0.15% power, and a bandpass emission filter of 570-660 nm. Time-lapse imaging was performed with 1h time resolution using the Zen Black 2.3 SP1 software v14.0.15.201 and

MyPic VBA macro[38]. XZ images of the dish surface reflection was acquired and processed by the MyPic VBA macro to define axial position for z-stack acquisition at each time point. Each stack was post-processed in Fiji[39]. Briefly, channels were split, maximum intensity projections produced, channels combined into a single image per time point, and all time points combined into a movie stack.

Zeiss Airyscan microscopy

AiryScan microscopy of RPE1 cells on patterned grids (Fig. 2a) was performed on a Zeiss LSM 880 AiryScan microscope (Carl Zeiss, Jena, Germany), using an AiryScan detector and a C-Apochromat 40x (NA 1.2) water immersion objective. Optimal sampling conditions for AiryScan acquisitions were achieved by selecting SR (super-resolution) scanning modality. Pixel size of 50 nm, and a 225 nm z step (total z-depth: 10-15 μm). Pixel dwell time: 0.64-1.18 μs. Master gain: 850-900. LifeAct-GFP was detected using a 488 nm line of Argon laser with a power of 1.5-2 % and a 495-550 nm bandpass emission filter. Stack datasets were post-processed in Zen Black 2.3 SP1 software v14.0.15.201 (Zeiss) to combine the multiple Airyscan 32-detector array images into deconvolved final images with high SNR and resolution.

Widefield microscopy imaging

Epifluorescence images (Fig. 2d inset, Supplementary Fig. 2) were recorded using a Zeiss Axio Observer.Z1 widefield microscope (Carl Zeiss, Jena, Germany) with an AxioCam MRm CCD camera, a A-Plan 10x (NA 0.25) Ph1 and a LD-Plan Neofluar 20x (NA 0.4) Ph2 Corr objectives. GFP was imaged with a 38 HE filter set and mCherry with a 43 HE filter set. Cells were imaged at 37°C and 5 % CO_2 with the Zen (blue edition) 2.3 software v2.3.69.1000. Images were processed (histogram adjusted and cropped) in Fiji.

Vitrification

Grids were blotted from the reverse side of the film and immediately plunged into a liquid ethane or ethane/propane mixture at liquid nitrogen temperature using a Leica EM GP plunger (Leica Microsystems, Vienna, Austria). The plunger was set to 37°C, 99 % humidity, and blot time of 2 s for R2/1, R2/2 and 2.5 s for R1/4 and R1.2/20 grids. The frozen grids were stored in sealed boxes in liquid nitrogen until further processing.

Cryo-scanning electron microscopy and focused ion beam milling

Cryo-FIB lamella preparations was performed as described in[5], on a dedicated Aquilos dual-beam microscope equipped with a cryo-transfer system and a cryo-stage (ThermoFisher Scientific, Brno, Czech Republic). Plunge frozen grids were fixed into autogrids modified for FIB preparation (a generous gift from the Max Planck institute of Biochemistry, Martinsried, Germany), mounted into a shuttle (ThermoFisher Scientific, Brno, Czech Republic) and transferred into the dual-beam microscope via a load-lock system. During FIB operation, samples were kept at constant liquid nitrogen temperature using an open nitrogen-circuit, 360° rotatable cryo-stage. To improve sample conductivity and reduce curtaining artifacts during FIB milling, the samples were first sputter-coated with platinum *in situ* (10 mA, 20 s), and then coated with organometallic platinum using the *in situ* gas injection

system (GIS, ThermoFisher Scientific, Eindhoven, Netherlands) operated at room temperature, 10.6 mm stage working distance and 7 s gas injection time. Appropriate positions for FIB preparations were identified and recorded in the MAPS 3.3 software (ThermoFisher Scientific, Brno, Czech Republic), and the eucentric height refined per position. Lamellae or wedges were prepared using Gallium ion beam at 30 kV, stage tilt angles of 20° for lamellae and 12°-13° for wedges. Lamella or wedge preparations were conducted in a stepwise manner, starting 5 μm away from the area of interest with currents of 1 nA, gradually reduced to a current of 50 pA for the final cleaning steps. Progress of the milling process was monitored using the scanning electron beam operated at 10 keV and 50 pA (or 2 keV for visualization of micropatterns). For improved conductivity of the final lamella for specimens intended for phase plate tomography, we again sputter coated the grid after cryo-FIB preparation with platinum (10 mA, 3 s). Grid were stored in sealed boxes in liquid nitrogen until further processing.

Cryo-electron tomography

Cryo-electron microscopy data were collected on a Titan Krios microscope operated at 300 kV (ThermoFisher Scientific, Eindhoven, Netherlands) equipped with a field-emission gun, a Quantum post-column energy filter (Gatan, Pleasanton, CA, USA), a K2 Summit direct detector camera (Gatan) and a Volta phase plate (ThermoFisher Scientific, Eindhoven, Netherlands). Data were recorded in dose-fractionation mode using acquisition procedures in SerialEM software v3.7.2[40]. Prior to the acquisition of tilt-series, montages of the grid squares or lamella were acquired at ~2 nm/pix. Tilt-series using a dose symmetric scheme[41] were collected in nano-probe mode, EFTEM magnification 42,000x corresponding to pixel size at the specimen level of 3.37 Å, 3-4 μm defocus, tilt increment 2° with constant dose for all tilts, total dose ~ 120 e$^-$/Å^2. The pre-tilt of lamellae with respect to the grid plane due to cryo-FIB milling at shallow angles (10-15°) was corrected for by tilting the stage on the microscope. Conventional tilt-series, without Volta phase plate (VPP), were acquired with an objective aperture and a beam tilt of 4 mrad for autofocusing (tomograms in Fig. 2e and 2f; Supplementary Fig. 5). A fraction of the tomographic tilt-series was acquired with the VPP (tomograms in Fig. 1g and Fig. 2j, k). Alignment and operation of the VPP were essentially carried out as described previously, applying a beam tilt of 10 mrad for autofocusing[4]. For conventional defocus data, a total of 30 tomograms were acquired on the peripheral areas of 13 micropatterned cells (from all micropattern designs shown in Fig. 2b). A total of 31 VPP tomograms were acquired from 8 wedges, equivalent to 8 cells grown on crossbow-, cross-, dumbbell-, oval-, and disk-shape micropatterns.

Data processing

Prior to tilt-series alignment, the projection movies were corrected for beam induced drift in the SerialEM plugin. Tilt series alignment and tomographic reconstructions were performed using the IMOD software package v 4.9.0[40]. In absence of fiducial gold nanoparticles in the FIB-lamellae or wedges, alignment of tilt-series images was performed with patch-tracking. Final alignment of the tilt-series images was performed using the linear interpolation option in IMOD without contrast transfer function (CTF) correction. Aligned images were binned to the final pixel size of 13.48 Å. For tomographic reconstruction, the radial filter options were left at their default values (cut off, 0.35; fall off, 0.05). Tomograms from Fig. 2e and

Supplementary Fig. 5d were treated with an anisotropic nonlinear diffusion denoising algorithm implemented in IMOD.

Statistics and Reproducibility

Experiments performed in Fig. 1a-b and 1e-g, Fig. 2a and 2g-k, Supplementary Fig. 2a-b and 2e-f, Supplementary Fig. 3a-j, Supplementary Fig. 6a and 6c-e, Supplementary Fig. 7a-d, and Supplementary Video 4 were performed independently three times with similar results.

Experiments from Fig. 1c-d and Supplementary Video 1 were performed once in a non-patterned and a patterned grid, time lapses were collected in five areas of the patterned grid, each area covering multiple grid squares.

Experiments from Fig. 2b-f, Supplementary Fig. 4a-c, Supplementary Fig. 5a-m, and Supplementary Videos 2-3, were performed in triplicate (three grids), collecting tomographic data from only one grid, resulting in 30 tomograms from 13 cells. Imaging by FIB-SEM of patterned grids (with laser 355 nm) in Supplementary Fig. 2c-d was performed only once. Experiments in Supplementary Fig. 2g-j was independently performed twice. In the Supplementary Fig. 3k, one grid (out of three grids) was used for cellular thinning by cryo-FIB milling.

Supplementary Material

Refer to Web version on PubMed Central for supplementary material.

Acknowledgements

Data availability

The authors declare that the data supporting the findings of this study are available within the paper and its supplementary information files. The raw data are available from the corresponding author upon reasonable request.

References

1. Kühlbrandt W. Science. 2014; 343:1443–1444. DOI: 10.1126/science.1251652 [PubMed: 24675944]

2. Pfeffer S, Mahamid J. Curr Opin Struct Biol. 2018; 52:111–118. DOI: 10.1016/j.sbi.2018.08.009 [PubMed: 30339965]

3. Beck M, Baumeister W. Trends Cell Biol. 2016; 26:825–837. DOI: 10.1016/j.tcb.2016.08.006 [PubMed: 27671779]

4. Mahamid J, et al. Science. 2016; 351:969–972. DOI: 10.1126/science.aad8857 [PubMed: 26917770]

5. Schaffer M, et al. J Struct Biol. 2017; 197:73–82. DOI: 10.1016/j.jsb.2016.07.010 [PubMed: 27444390]

6. Rigort A, et al. Proc Natl Acad Sci U S A. 2012; 109:4449–4454. DOI: 10.1073/pnas.1201333109 [PubMed: 22392984]

7. Wang K, Strunk K, Zhao G, Gray JL, Zhang P. J Struct Biol. 2012; 180:318–326. DOI: 10.1016/j.jsb.2012.07.003 [PubMed: 22796867]

8. Hariri H, et al. J Cell Biol. 2019; 218:1319–1334. DOI: 10.1083/jcb.201808119 [PubMed: 30808705]

9. Ader NR, et al. Elife. 2019; 8doi: 10.7554/eLife.40712

10. Khanna K, et al. Elife. 2019; 8doi: 10.7554/eLife.45257

11. Weiss GL, Kieninger AK, Maldener I, Forchhammer K, Pilhofer M. Cell. 2019; 178:374–384 e315. DOI: 10.1016/j.cell.2019.05.055 [PubMed: 31299201]

12. Jasnin M, Ecke M, Baumeister W, Gerisch G. Structure. 2016; 24:1031–1043. DOI: 10.1016/j.str.2016.05.004 [PubMed: 27320835]

13. Asano S, Engel BD, Baumeister W. J Mol Biol. 2016; 428:332–343. DOI: 10.1016/j.jmb.2015.09.030 [PubMed: 26456135]

14. Förster F, Hegerl R. Methods Cell Biol. 2007; 79:741–767. DOI: 10.1016/S0091-679X(06)79029-X [PubMed: 17327182]

15. Guo Q, et al. Cell. 2018; 172:696–705 e612. DOI: 10.1016/j.cell.2017.12.030 [PubMed: 29398115]

16. Bäuerlein FJB, et al. Cell. 2017; 171:179–187 e110. DOI: 10.1016/j.cell.2017.08.009 [PubMed: 28890085]

17. Patla I, et al. Nat Cell Biol. 2010; 12:909–915. DOI: 10.1038/ncb2095 [PubMed: 20694000]

18. Marston DJ, et al. Proc Natl Acad Sci U S A. 2019; 116:1267–1272. DOI: 10.1073/pnas.1808830116 [PubMed: 30630946]

19. Siegmund SE, et al. iScience. 2018; 6:83–91. DOI: 10.1016/j.isci.2018.07.014 [PubMed: 30240627]

20. Sorrentino S, Studt JD, Horev MB, Medalia O, Sapra KT. Cell Adh Migr. 2016; 10:568–575. DOI: 10.1080/19336918.2016.1173803 [PubMed: 27104281]

21. Tamir A, et al. J Struct Biol. 2016; 193:181–187. DOI: 10.1016/j.jsb.2015.12.013 [PubMed: 26767592]

22. Hampton CM, et al. Nat Protoc. 2017; 12:150–167. DOI: 10.1038/nprot.2016.168 [PubMed: 27977021]

23. Mader A, Elad N, Medalia O. Methods Enzymol. 2010; 483:245–265. DOI: 10.1016/S0076-6879(10)83012-5 [PubMed: 20888478]

24. Maimon T, Elad N, Dahan I, Medalia O. Structure. 2012; 20:998–1006. DOI: 10.1016/j.str.2012.03.025 [PubMed: 22632834]

25. Azioune A, Carpi N, Tseng Q, Thery M, Piel M. Methods Cell Biol. 2010; 97:133–146. DOI: 10.1016/S0091-679X(10)97008-8 [PubMed: 20719269]

26. Thery M. J Cell Sci. 2010; 123:4201–4213. DOI: 10.1242/jcs.075150 [PubMed: 21123618]

27. Strale PO, et al. Adv Mater. 2016; 28:2024–2029. DOI: 10.1002/adma.201504154 [PubMed: 26689426]

28. Booy FP, Pawley JB. Ultramicroscopy. 1993; 48:273–280. [PubMed: 8475597]

29. Thery M, Jimenez-Dalmaroni A, Racine V, Bornens M, Julicher F. Nature. 2007; 447:493–496. DOI: 10.1038/nature05786 [PubMed: 17495931]

30. Thery M, et al. Nat Cell Biol. 2005; 7:947–953. DOI: 10.1038/ncb1307 [PubMed: 16179950]

31. Arnold J, et al. Biophys J. 2016; 110:860–869. DOI: 10.1016/j.bpj.2015.10.053 [PubMed: 26769364]

32. Engel L, et al. J Micromech Microeng. 2019; 29

33. Thery M, et al. Proc Natl Acad Sci U S A. 2006; 103:19771–19776. DOI: 10.1073/pnas.0609267103 [PubMed: 17179050]

34. Senger F, et al. 2019; Spatial integration of mechanical forces by α-actinin establishes actin network symmetry. J. Cell Sci. doi: 10.1242/jcs.236604

35. Jasnin M, Crevenna AH. Biophys J. 2016; 110:817–826. DOI: 10.1016/j.bpj.2015.07.053 [PubMed: 26497103]

36. Toro-Nahuelpan M, et al. Protocol Exchange. 2019; doi: 10.21203/rs.2.12377/v1

37. Vignaud T, et al. J Cell Sci. 2012; 125:2134–2140. DOI: 10.1242/jcs.104901 [PubMed: 22357956]

38. Politi AZ, et al. Nat Protoc. 2018; 13:1445–1464. DOI: 10.1038/nprot.2018.040 [PubMed: 29844523]

39. Schindelin J, et al. Nat Methods. 2012; 9:676–682. DOI: 10.1038/nmeth.2019 [PubMed: 22743772]

40. Kremer JR, Mastronarde DN, McIntosh JR. J Struct Biol. 1996; 116:71–76. DOI: 10.1006/jsbi.1996.0013 [PubMed: 8742726]

41. Hagen WJH, Wan W, Briggs JAG. J Struct Biol. 2017; 197:191–198. DOI: 10.1016/j.jsb.2016.06.007 [PubMed: 27313000]

Editor's summary

Micropatterning of cryo-EM grids enables controlled adhesion of mammalian cells for cryoET-based structural studies. This approach leads to reproducible cellular morphology and improves FIB thinning of cells for in-cell structural analyses.
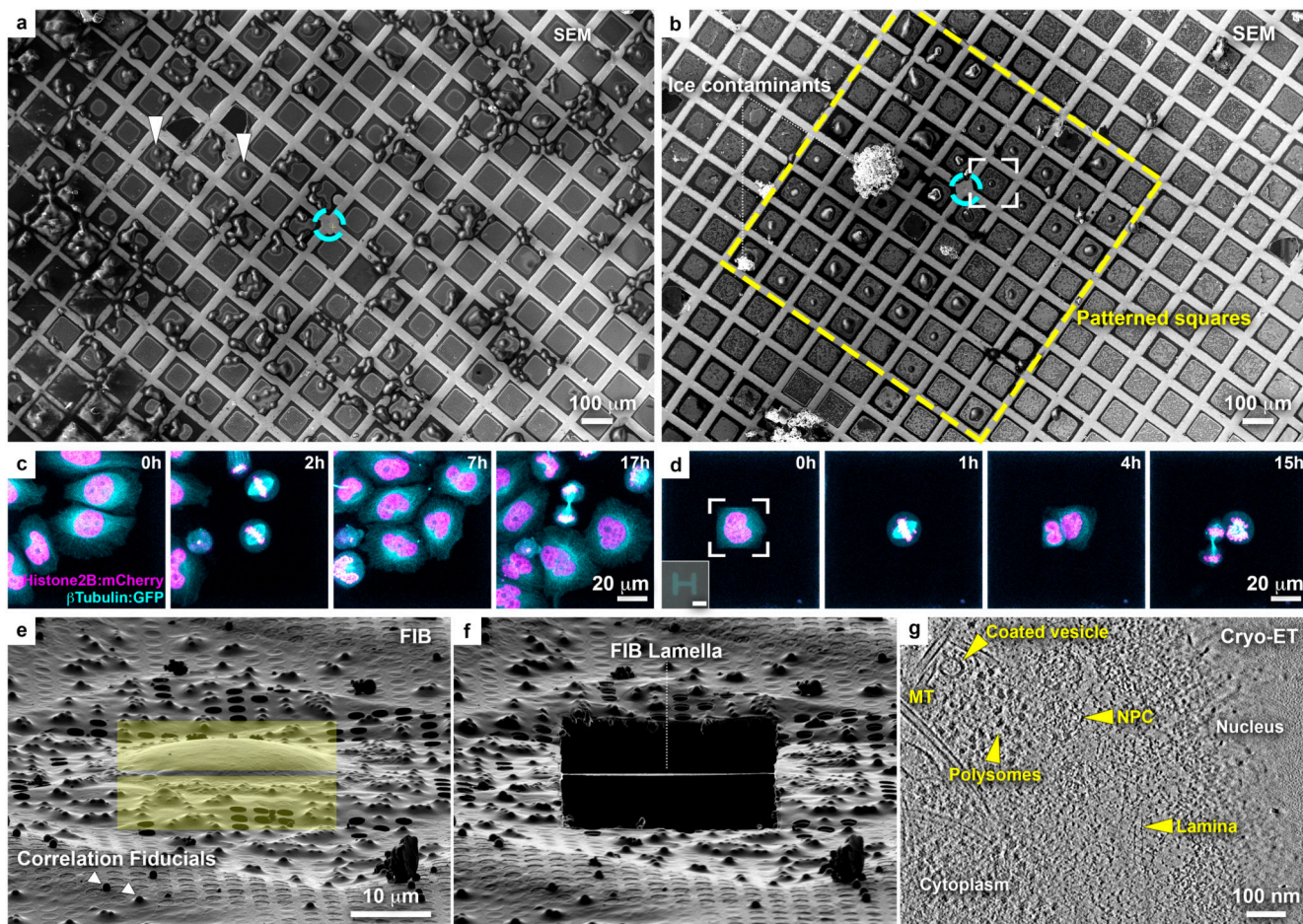
Figure 1. Micropatterning of cryo-EM grids refines preparation for cryo-FIB lamella micromachining from adherent mammalian cells.
(a) Cryo-scanning electron micrograph (SEM) of HeLa cells grown overnight on a gold-mesh grid with a holey (R2/1) SiO_2 film. Cyan circle indicates grid center. Only a small fraction of the cells is optimally positioned for FIB-lamellae preparation (arrowheads). (b) HeLa cells grown overnight on a gold-mesh grid coated with a holey (R2/1) carbon film micropatterned with 20 μm diameter disks on 8 x 8 grid squares (yellow rectangle) around the grid center (cyan circle) and treated with fibronectin. (c, d) HeLa cells, expressing GFP-tagged β-tubulin (Cyan) and mCherry-tagged histone (H2B: magenta), seeded on a (c) control and (d) patterned gold-mesh grids with SiO_2 (R1.2/20) holey film. Inset: H-shaped pattern induced the square cell shape. Scale: 20 μm. Cell-cycle was synchronized with a single Thymidine block (16 h), released into fresh medium (8h), followed by overnight live-cell imaging. A field of view of a single grid square is shown for both (c) and (d). Cells continue dividing ~40 h post-seeding (see Supplementary Video 1). (e) FIB shallow angle view on cell framed in (b). Yellow rectangles indicate patterns for milling. Correlation fiducials (microbeads; arrowheads) can facilitate 3D-targeted cryo-FIB preparations. (f) Lamella produced from cell in (e). (g) Tomographic slice, 6.8 nm thickness, of the nuclear periphery of the cell in (e). Lamella thickness determined from the tomographic reconstruction was 90 nm. NPC: nuclear pore complex; MT: microtubule.
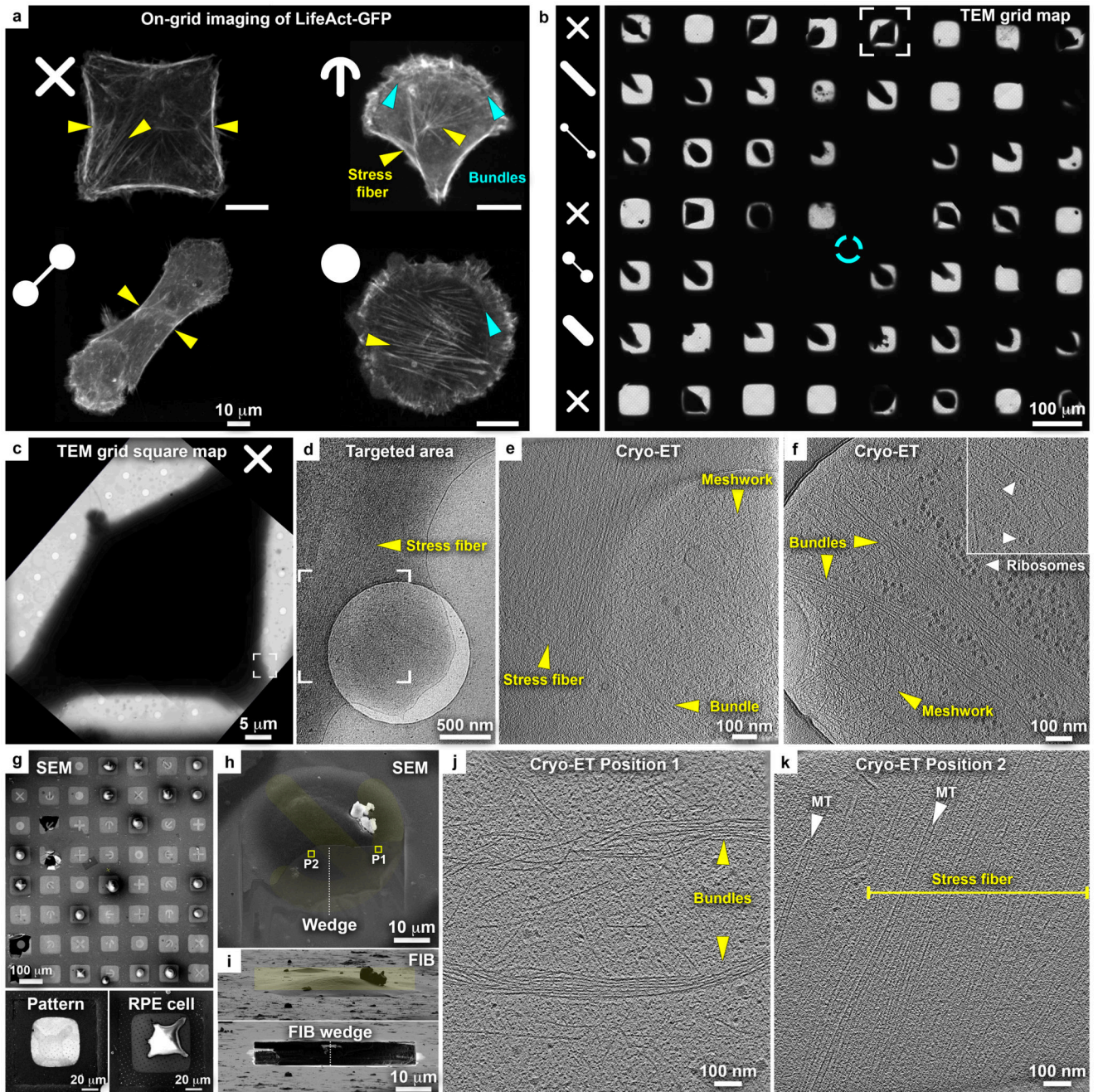
Figure 2. Cryo-EM grid micropatterning tailored for controlling cellular morphology and cytoskeletal architecture.

(a) On-grid (gold-mesh, SiO_2 film R1/4) live-cell confocal microscopy of the actin organization in RPE1 LifeAct-GFP cells grown on complex micropatterns. Pattern designs are indicated at the top left of each of the light microscopy images. Positioning of actin stress fibers (yellow arrowheads) correlates with the distinct patterns. Blue arrowheads: actin bundles arranged into an arc or ring structure. **(b-f)** Cellular cryo-ET of RPE1 cells in peripheral thin regions (gold-mesh, SiO_2 film R1/4). **(b)** Cryo TEM map of grid with 8 x 7

patterned grid squares. Patterns per row are indicated (left column). Cyan circle: grid center. **(c)** Cryo-TEM micrograph of a grid square of the framed cell in (b) grown on a cross-shaped pattern. **(d)** Magnified cryo-TEM micrograph of the framed area in (c), targeted for tomography. **(e)** Tomographic slice of the specified area in (d), 6.8 nm thickness, showing the organization of actin filaments into a stress fiber and an isotropic meshwork in the adjacent cellular protrusion. For full tomogram, see Supplementary Video 2. **(f)** Tomographic slice of the periphery of another cell grown on an oval-shape pattern depicting actin meshwork, bundles, and unidentified hexameric macromolecular complexes in the vicinity of the basal and apical cell membranes (inset: arrowheads). For full tomogram, see Supplementary Video 3. **(g-k)** Cellular thinning by cryo-FIB followed by cryo-ET. **(g)** SEM of RPE1 cells on a patterned titanium-mesh (SiO$_2$ film R1.2/20) grid and overlaid with an image of the patterns. Bottom panels: gold-mesh, SiO$_2$ film R1/4 grid. Left: 2 keV SEM image of a cross-shaped micropatterned grid square. Right: SEM of RPE1 cell spreading on a cross-shaped pattern. **(h)** SEM of a cell grown on a crossbow-shaped pattern (yellow) overlaid with the SEM micrograph of a wedge (top view) produced by cryo-FIB milling (titanium-mesh, SiO$_2$ film R1.2/20). Squares indicate the positions of tomographic slices in (j) and (k). **(i)** Upper panel: FIB shallow angle view on cell in (h). Yellow rectangle indicates the pattern for milling. A thin wedge at the basal cell membrane is produced by ablating the top of the cell. Lower panel: cell after milling. **(j, k)** Tomographic slices of positions 1 and 2 indicated in (h). Actin bundles likely equivalent to actin transverse arcs (j) and internal stress fibers (k) are found in locations expected according to the actin map in a crossbow-shaped RPE1 cell (a).